https://doi.org/10.5194/wes-2026-79
Preprint. Discussion started: 29 May 2026

WIND ENERGY SCIENCE DISCUSSIONS
Open Access

UAV-based infrared thermography for laminar–turbulent transition detection on wind turbines in operation: quantifying motion-blur effects using blade image velocity

Lennart Rackwitz[1], Nils Poeck[2], Nicholas Balareque[2], Axel von Freyberg[1], and Andreas Fischer[1,3]

[1]University of Bremen, Bremen Institute for Metrology, Automation and Quality Science (BIMAQ), Bremen, Germany
[2]Deutsche WindGuard Engineering GmbH, Bremerhaven, Germany
[3]MAPEX Center for Materials and Processes, University of Bremen, Bremen, Germany

Correspondence: Lennart Rackwitz (l.rackwitz@bimaq.de)

Abstract. This study investigates the applicability of uncrewed aerial vehicle (UAV)-based infrared thermography (IRT) for aerodynamic flow visualization on operating wind turbines, with a focus on the localization of the laminar–turbulent transition. While UAV deployment enables flexible, non-contact measurements at large stand-off distances, the use of lightweight microbolometer cameras introduces limitations related to temporal response and motion blur induced by high blade image velocity. A Gaussian error-function-based approach is employed to localize blade edges and transition features in thermographic images. Controlled laboratory experiments are conducted to isolate the influence of motion blur over a wide range of blade image velocities. The results show that increasing blade image velocity leads to a progressive broadening of temperature gradients and a corresponding increase in localization uncertainty. At high image velocities, the underlying intensity profiles deviate from the assumed model shape, resulting in a marked loss of robustness in the edge-detection procedure. To mitigate these effects, image deblurring based on Wiener deconvolution is applied using a point-spread function derived from the exponential response of the microbolometer detector. The deblurring approach significantly improves the stability of the evaluation and reduces the transition-location uncertainty by approximately a factor of five at high blade image velocities. The methodology is further applied to field measurements on a $1.5\,\mathrm{MW}$ wind turbine. The results demonstrate that transition-related thermal signatures can be detected under operational conditions and that deblurring substantially enhances the visibility of flow features, particularly in regions of high blade image velocity. Field-based uncertainty estimates further show that, at high blade image velocities, deviations from the assumed signal model become the dominant source of error, while deblurring primarily improves the robustness of the transition localization rather than uniformly reducing uncertainty. Thus, the findings identify motion blur as the dominant limitation for quantitative UAV-based IRT measurements and demonstrate that its impact can be effectively reduced by appropriate post-processing. The presented approach provides a framework for estimating motion-blur-induced uncertainty and defines practical limits for transition localization in airborne thermographic measurements.

1 Introduction

1.1 Motivation

With the rising global demand for renewable energy, wind energy continues to be a low-carbon, cost-competitive resource. Global installed offshore capacity increased by $157\,\%$ from 28.29 GW to 72.66 GW between 2019 and 2023 (Jung et al., 2024). The efficiency of modern wind turbines in converting wind into electrical power is strongly influenced by the aerodynamic performance of their rotor blades. Especially the position of the transition between the laminar and turbulent flow regimes within the boundary layer is important as it stands in direct correlation to the lift and drag of the blades (Schlichting and Gersten, 2017). Therefore, a detailed understanding and an evaluation of the actual flow on operating wind turbines are essential additions to numerical flow simulations with regard to the development and optimization of the turbine's rotor blades. Since wind turbines achieve heights up to $200\,\mathrm{m}$ and are expected to increase further in size, a flow inspection method is demanded that can access the required heights, requires no modification of the wind turbine, and works contactless during operation. Furthermore, airborne inspection methods are desirable for the future applicability on offshore wind turbines.

1.2 State of the Art

Visualization of the boundary-layer flow on wind-turbine blades is achievable with surface markers, embedded instrumentation, and remote optical diagnostics. Oil films are used to trace near-wall shear and separation and reattachment lines but require careful surface preparation and post-test cleanup (Medina et al., 2011b; Li et al., 2016), even when environmentally sustainable formulations are used (Medina et al., 2011a). Tufts (short yarn or polymer filaments) qualitatively indicate local flow direction and unsteadiness (Vey et al., 2014; Oehme et al., 2022a), while stall flags are dedicated markers for separated regions. Both demand dense installation and require labor-intensive image interpretation to extract flow information on rotating geometries (Li et al., 2016). Among embedded methods, pressure taps or transducers provide surface-pressure distributions, and hot-film sensors yield local skin-friction and transition information. However, surface markers and embedded instrumentation are invasive to the blade surface and entail substantial preparation and calibration (Schaffarczyk et al., 2017).

Within remote optical diagnostics, Particle Image Velocimetry (PIV) delivers planar velocity fields in the near-surface flow and has been widely applied to airfoils in wind-tunnel experiments (Burgmann et al., 2006) and rotating model turbines (Herráez et al., 2018) but its reliance on tracer seeding, synchronized high-power illumination, and multi-camera optics effectively makes the application on full-scale, in-operation wind turbines impractical. Pressure- and temperature-sensitive paints (PSP/TSP) provide global, high-resolution surface pressure or temperature maps for transition and load studies in controlled laboratory environments and wind tunnel experiments (Costantini et al., 2021; Liu et al., 2021). However, they require dedicated surface coatings, controlled illumination, and careful calibration, which limits their use on operational rotors. Collectively, these techniques are powerful in laboratories or prepared field campaigns but entail substantial installation effort, downtime, and potential flow disturbance – motivating non-contact alternatives suitable for routine, in-operation use at a high altitude onshore and potentially offshore.

An in-process capable flow inspection method, which requires no modification of the rotor blade and works contactless, is infrared thermography (IRT). Ground-based IRT measurements using cooled photon detectors have been extensively studied and are commonly used in industry and research (Chaudhuri et al., 2024; Dorszewski et al., 2024; Gleichauf et al., 2023; Traphan et al., 2018). Its aerodynamic capability spans the localization of the laminar–turbulent transition in wind-tunnel studies on helicopter rotor blades (Gleichauf et al., 2020), on aircraft airfoils (Gartenberg et al., 1992), and on wind-turbine blades (Gleichauf et al., 2021; Reichstein et al., 2019). Unsteady flow features have likewise been resolved, including laminar separation (Montelpare and Ricci, 2004) and dynamic stall in both wind-tunnel and operating-turbine environments (Oehme et al., 2022b).

For transition visualization, the measurement quality is commonly expressed by the contrast-to-noise ratio (CNR). Using stationary systems, Dollinger et al. (2018) demonstrated reliable laminar-turbulent transition detection. Beyond the use of the CNR, the uncertainty of laminar–turbulent transition localization was investigated and achieved sub-pixel accuracy of $0.17\,\%$ relative to the rotor blade chord length. Fixed platforms of ground-based measurements, however, are constrained by line-of-sight and site logistics, limiting flexibility – particularly offshore.

To extend accessibility, Galleguillos et al. (2015) demonstrated uncrewed aerial vehicle (UAV) based IRT for qualitative blade inspection focused on composite defects. While confirming feasibility, this work did not address quantitative flow analysis or uncertainty. A more recent review by Chen et al. (2025) provides a comprehensive overview of in-process flow visualization techniques for wind turbines in operation. While the review acknowledges the potential of UAV-based IRT, it highlights a significant research gap regarding the quantitative characterization of measurement quality under real operational conditions. The outstanding issues from UAV-specific factors occur such as motion and vibration of the platform as well as limited focus and integration-time of the used lighter camera technology. Especially, given the high relative blade speed and the fixed integration time with rolling readout of the camera sensor, motion blur is expected, reducing effective spatial resolution and directly constraining quantitative flow visualization from UAVs. As a result, the actual measurement capabilities of UAV-based flow visualization needs clarification.

1.3 Aim

The aim of this study is to design, characterize, and further develop a UAV-based IRT system for aerodynamic flow visualization on wind turbine blades in operation, with a particular focus on the detection and localization of the laminar–turbulent transition. The influence of thermal, spatial, and temporal resolution of lightweight microbolometer cameras on flow visualization capability is systematically investigated. Special emphasis is placed on quantifying motion blur induced by the relative image velocity between rotor blade and camera, on assessing image de-blurring techniques in post-processing to mitigate these effects, and on exploring the resulting impact on measurement uncertainty. Based on controlled laboratory experiments and in-field measurements, an attempt is made to quantify the achievable uncertainty of the laminar–turbulent transition position and to define operational limits for UAV-based IRT under realistic measurement conditions. The performance of the system is finally demonstrated on a $1.5\,\mathrm{MW}$ wind turbine under operational conditions.

https://doi.org/10.5194/wes-2026-79
Preprint. Discussion started: 29 May 2026

2 Measurement Principle and UAV-related challenges

Thermographic flow visualization is based on variations in convective heat transfer within the boundary layer of aerodynamic surfaces. Different flow states, such as laminar, turbulent, or separated flow, are associated with distinct local heat transfer coefficients, which result in measurable differences in surface temperature provided a temperature difference exists between the airfoil and the surrounding medium. By recording surface temperature distributions using IRT, it is therefore possible to differentiate boundary-layer flow regimes on wind turbine blades in operation (Joseph et al., 2016). In practical applications, the laminar–turbulent transition manifests as a localized change in surface temperature along the blade surface, caused by the increase in convective heat transfer when the boundary layer becomes turbulent. This temperature gradient is typically observed as a distinct line or band in infrared thermograms and can be extracted using profile-based evaluation methods to determine the transition location along the chord axis.

2.1 UAV-based detection of laminar-turbulent transition with IRT

When applied from an uncrewed aerial vehicle, the thermographic detection of the laminar–turbulent transition follows the same physical principles as in ground-based measurements. The UAV-based approach and an example thermogram are schematically shown in Fig. 1. The infrared camera observes the rotating blade from a finite stand-off distance while the camera is carried by a moving platform, i.e. the UAV. To assess the boundary layer flow conditions in the images, the intensity profiles are evaluated along the y-axis of the intensity distributions as shown schematically in Fig. 2. Leading edge, trailing egde and transition localization is each performed using an approximation with a Gaussian error function model adapted from Dollinger et al. (2018). The normalized intensity profile across an edge or transition is modeled as

$$I(y) = \hat{a}\,\mathrm{erf}\left(\frac{y-\hat{b}}{\sqrt{2}\,\hat{w}}\right) + \hat{d}, \tag{1}$$

where $\hat{a}$ denotes the intensity contrast across the edge, $\hat{b}$ the inferred position of the edge or transition, $\hat{w}$ the characteristic width of the temperature gradient, and $\hat{d}$ an intensity offset. Applying Eq. (1) to the leading edge (LE), trailing edge (TE), and laminar–turbulent transition (LTT) yields the respective fitted positions $\hat{b}_{\mathrm{LE}}$, $\hat{b}_{\mathrm{TE}}$, and $\hat{b}_{\mathrm{LTT}}$. The apparent chord length in image coordinates is here defined as

$$c = \hat{b}_{\mathrm{TE}} - \hat{b}_{\mathrm{LE}}. \tag{2}$$

The transition location relative to the leading edge is then obtained by calculating

$$\theta = \hat{b}_{\mathrm{LTT}} - \hat{b}_{\mathrm{LE}}, \tag{3}$$

and the relative transition position along the chord thus is

$$\frac{\theta}{c} = \frac{\hat{b}_{\mathrm{LTT}} - \hat{b}_{\mathrm{LE}}}{\hat{b}_{\mathrm{TE}} - \hat{b}_{\mathrm{LE}}}. \tag{4}$$

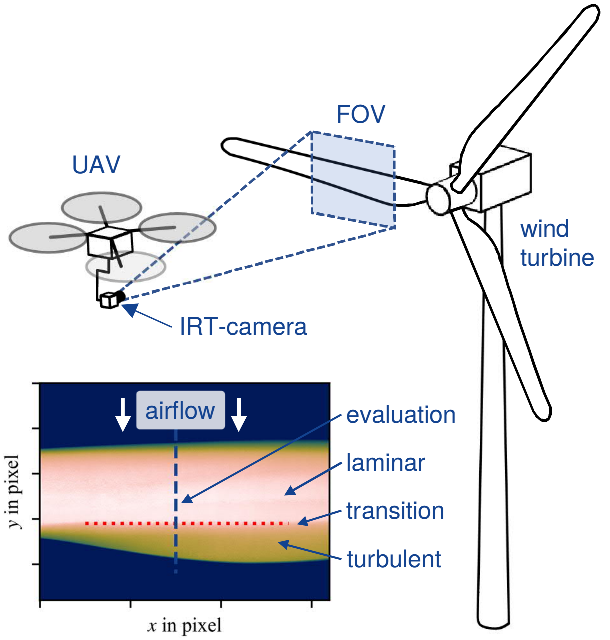

Figure 1. Schematic of a UAV-based IRT measurement in front of a wind turbine and an example thermogram of a rotating rotor blade. The laminar–turbulent transition is displayed with a dotted red line while a blue dashed line represents an example intensity profile for evaluation. Colours in this and subsequent figures use the `batlowW` Scientific colour map (Crameri, 2018)

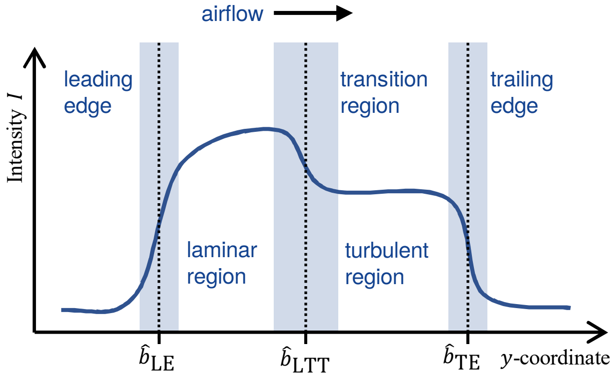

Figure 2. Schematic intensity profile along the y-coordinate of an infrared image of a wind turbine rotor blade. The approximated positions of the leading egde, laminar–turbulent transtion and trailing edge are denoted with $\hat{b}_{\mathrm{LE}}$, $\hat{b}_{\mathrm{Tr}}$ and $\hat{b}_{\mathrm{TE}}$ respectively.

While fitting edge or transition positions with the Gaussian error function enables sub-pixel localization along the image profile coordinate, the extracted positions require careful interpretation in blade coordinates. In the present evaluation, the chordwise extent c at a given spanwise location is obtained from the difference between the fitted leading and trailing edge positions, i.e. from the apparent edge locations in the image. For practical interpretation, however, the fitted parameters $\hat{b}$ must be mapped to the physical blade geometry. Without accurate geometric information, perspective and projection effects cannot be fully corrected, which may introduce systematic deviations in the inferred transition position (Fischer et al., 2023). This challenge is particularly pronounced for UAV-based measurements, where the observation platform is not fixed and variations in stand-off distance and viewing angle can occur during operation. Since no geometric reference data of the blade are available for the present measurements, the analysis concentrates on the robustness and limits of the edge-detection model under motion-blur conditions introduced by the imaging system, rather than on absolute geometric reconstruction.

On the one hand, a UAV allows the measurement system to adapt to changes in turbine yaw during operation, whereas ground-based setups typically require physical relocation of the sensor, which can be impractical or infeasible under field conditions. On the other hand, a UAV means constrained payload and power resources, which is crucial for the choice of the camera. In conventional ground-based IRT measurements, systems equipped with cooled photon detectors are commonly employed to achieve high thermal sensitivity and temporal resolution, enabling detailed flow visualization and reliable localization of the laminar–turbulent transition. However, the associated requirements in terms of payload and power consumption restrict their applicability on UAV platforms. UAV-based IRT therefore usually relies on lightweight uncooled microbolometer focal plane array cameras, which offer reduced mass and power consumption but at the expense of thermal sensitivity and dynamic response. Transition detection from UAV-based IRT requires careful consideration of how sensor characteristics and blade image motion influence the thermographic transition signature.

2.2 Measurement challenges of UAV-based IRT

While the physical principle of thermographic transition detection remains unchanged for UAV-based measurements, two fundamental challenges arise from the airborne implementation. First, the relative motion between rotor blade and imaging system results in high apparent motion of temperature gradients in the image plane. Second, the use of lightweight uncooled microbolometer cameras instead of cooled photon detectors affects the capabilities of the image acquisition system in terms of sensitivity, temporal and spatial resolution.

Although cooled photon detectors typically achieve lower noise-equivalent temperature differences, modern microbolometer systems provide comparable thermal sensitivity for many flow-visualization applications. For transition detection under airborne conditions, temporal effects associated with the sensor's temporal resolution are therefore expected to dominate over purely thermal noise limitations.

Microbolometer detectors have a comparatively large thermal time constant, which can be approximated by a first-order dynamic response to incident heat flux. In addition, most microbolometer focal plane arrays employ a rolling-shutter architecture in which detector rows are read out sequentially. For typical array sizes of 480×640 pixels and per-row integration times in the order of $30\,\mu\mathrm{s}$, the resulting effective fixed integration time is approximately $16\,\mathrm{ms}$. Cooled photon detector cameras commonly used in ground-based measurements, in contrast, employ global-shutter acquisition with adjustable integration times down to the microsecond range and substantially higher achievable frame rates, thereby reducing motion-induced blurring. Thus, in combination with the high relative motion between rotor blade and camera, the increased finite integration time can lead to a spatial smearing of temperature gradients in the recorded thermograms, broadening the apparent transition signature and reducing the steepness of the extracted intensity profiles.

Regarding spatial resolution, the spatial sampling of the blade surface depends on focal length and stand-off distance and can be of comparable magnitude for airborne and ground-based configurations. Optical distortions are inherent to both approaches and primarily depend on lens characteristics rather than platform type. UAV-based deployment may provide additional flexibility, for example by allowing adaptation to turbine yaw and adjustment of the viewing angle without relocating ground infrastructure. However, variations in stand-off distance and viewing geometry during flight can introduce additional geometric uncertainty in the mapping between image coordinates and physical blade coordinates, particularly if no synchronized geometric reference is available.

Taken together, the relative motion between blade and sensor and the temporal response characteristics of microbolometer detectors define the primary measurement constraints of UAV-based infrared thermography. Therefore, the influence of motion-induced effects on transition localization and how to cope with it in field measurements is investigated in detail.

3 Measurement system and experiments

This section describes the employed measurement system and the experimental procedures used in laboratory and in-field investigations.

3.1 Measurement system

3.1.1 Infrared Camera

All thermographic measurements are performed using a long-wave infrared (LWIR) camera module from InfraTec (model PIR uc 605), sensitive in the spectral range from $8\,\mu\mathrm{m}$ to $14\,\mu\mathrm{m}$. The camera is based on an uncooled microbolometer focal plane array with rolling shutter readout and a sensor resolution of 640×480 pixels at a pixel pitch of $17\,\mu\mathrm{m}$. At an operating temperature of 30°C, the manufacturer specifies a noise-equivalent temperature difference (NETD) of $\leq 60\,\mathrm{mK}$ for full-frame acquisition at a maximum frame rate of $25\,\mathrm{Hz}$ via Ethernet.

The camera module features manual focus and interchangeable optics and is housed in a compact and robust enclosure. Without the lens is has a mass of $110\,\mathrm{g}$ and external dimensions of $55.8 \times 44 \times 46\,\mathrm{mm}$. These characteristics make the system well suited for airborne operation. For the measurements reported in this study, the camera is equipped with a lens of focal length $50\,\mathrm{mm}$.

Radiometric operation is provided by a factory calibration over a temperature range from -20°C to 400°C. In the present experiments, the camera is operated in its factory-calibrated radiometric mode with a selected measurement range between -20°C and 135°C. Prior to each measurement run, a one-point non-uniformity correction (NUC) is applied to reduce fixed-pattern noise. The recorded temperature values are therefore interpreted in a relative sense and used to derive contrast-based flow metrics rather than absolute surface temperatures.

https://doi.org/10.5194/wes-2026-79
Preprint. Discussion started: 29 May 2026

3.1.2 Image processing

This subsection describes the general image-processing approach used for blade edge and flow transition detection in both laboratory and field measurements. Experiment-specific data processing and evaluation strategies follow in Section 3.2.

Prior to edge evaluation, all thermograms are cropped to a common region of interest to exclude irrelevant background regions. The images are then rotated such that the leading edge of the blade is aligned horizontally in the image plane. This alignment enables a column-wise analysis of intensity profiles approximately normal to the local blade edge and provides a consistent reference frame for subsequent evaluation. Profiles are averaged over a spanwise stripe to reduce noise, using 5 pixels in the laboratory data and 15 pixels in the field data.

The fitted blade-edge positions are used to derive the blade width as an estimate of the chord length from the difference between leading and trailing edge locations. In the laboratory experiments, no incoming wind exists, i.e. solely the localization of the blade edges is studied. In the field measurements the Gaussian error function model is also applied to the flow-induced temperature gradient associated with the laminar–turbulent transition. In both cases, the width parameter of the fitted Gaussian error function $\hat{w}$ serves as a measure of spatial spreading of the detected gradient and is used as an indicator of motion-induced image degradation.

All evaluations are related to the relative motion between blade and sensor, expressed as the blade image velocity, $v_{\mathrm{img}} = \omega r$, (in $\mathrm{pixel\,s^{-1}}$) where ω denotes the angular velocity of the rotor and r the radial position in the image. The formulation of relative motion as blade image velocity provides a common basis for comparing laboratory and field measurements with respect to motion-blur effects. Potential mitigation strategies based on image de-blurring and compensation of detector dynamics are not applied in the present processing chain and are addressed separately in Section 4.2.

3.1.3 UAV platform

The airborne measurement system is integrated into a hybrid uncrewed aerial vehicle (UAV) designed for long-endurance operation. A Hecto Drones HD-408 multirotor platform is employed, featuring an X8 configuration with eight non-foldable 21-inch carbon fiber propellers. The UAV is powered by an onboard generator with a nominal electrical output of $7\,\mathrm{kW}$ and a two-stroke fuel system with a $15\,\mathrm{l}$ tank. Two lithium-polymer batteries connected in series form a 12S safety battery system. The platform has a maximum take-off mass of $49\,\mathrm{kg}$ and a maximum payload capacity of up to $17\,\mathrm{kg}$. For the measurement configuration used in this study, typical flight times of approximately two to three hours are achieved.

The measurement payload is mounted on a Gremsy T7 gimbal, which provides active stabilization in pitch, roll, and yaw. The gimbal supports payload masses of up to $1.86\,\mathrm{kg}$ within a design envelope of $180 \times 130 \times 150\,\mathrm{mm}$ (width × height × depth). The infrared camera is rigidly attached to the gimbal and operated at a fixed frame rate of $25\,\mathrm{Hz}$. Image stabilization is achieved exclusively by the gimbal; no additional image-based stabilization is applied at this stage.

In addition to the infrared camera, the payload includes a LiDAR sensor (Livox AVIA) to provide range information during flight. The LiDAR operates at a wavelength of $\lambda = 905\,\mathrm{nm}$ with a nominal point rate of $240{,}000\,\mathrm{points\,s^{-1}}$. LiDAR data are recorded asynchronously and evaluated in post-processing to estimate the average stand-off distance between the UAV and

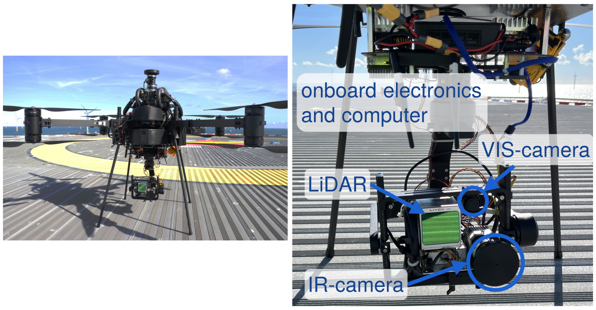

(a) (b)

Figure 3. UAV-based measurement platform. (a) Hybrid multirotor UAV used for the in-field measurements. (b) Close-up view of the measurement payload mounted on the gimbal, including the infrared camera, visible-light camera, LiDAR sensor, and onboard computer.

the measurement object. Furthermore, a monochromatic visible-light camera (The Imaging Source DMK 33GX545, resolution 4096×3000 pixels, pixel pitch $2.74\,\mu\mathrm{m}$) is also mounted on the gimbal. This camera provides visual feedback for piloting and documentation purposes. However, its recordings are not synchronized with the infrared data and are not used for quantitative analysis in the present study.

An overview of the UAV platform and a close-up view of the integrated measurement systems are shown in Fig. 3.

3.2 Experiments

3.2.1 Laboratory experiments

Aim of the experiment: The laboratory experiments are designed to quantitatively assess the influence of motion blur on thermographic edge localization under controlled and repeatable conditions. Rather than attempting to reproduce a physical laminar–turbulent transition, which would require a wind tunnel environment and is not well suited to isolating image motion effects, the experiments focus on characterizing the degradation of edge sharpness and positional uncertainty induced by blade motion. In this context, the trailing edge is used as a surrogate transition feature, providing a well-defined thermal gradient that resembles the virtual transition signature observed in infrared thermography of wind turbine blades. Consequently, the transition position is defined by $\hat{b}_{\mathrm{LTT}} \equiv \hat{b}_{\mathrm{TE}}$, so that the uncertainty of $\theta = \hat{b}_{\mathrm{LTT}} - \hat{b}_{\mathrm{LE}}$ due to the rotor motion effect can be studied.

Measurement object: The experiments are conducted using a three-bladed scaled wind turbine model with a hub height of $1.7\,\mathrm{m}$ and a blade length of $609\,\mathrm{mm}$. The rotor is positioned at a distance in front of a planar, thermally homogeneous background to generate a stable thermal contrast. The background consists of an aluminium plate with a thickness of $8\,\mathrm{mm}$, heated from the rear by an electrical heat source to ensure uniform surface temperature. Following established practice in thermographic transition studies, the metallic surface is covered with a self-adhesive matte black PVC foil (thickness $\leq 100\,\mu\mathrm{m}$) to increase emissivity and suppress thermal reflections while having a negligible influence on geometry (Traphan et al., 2018; Joseph et al., 2016; Reyer et al., 2006). The heat source is setup such that the thermal contrast between the blades and back-

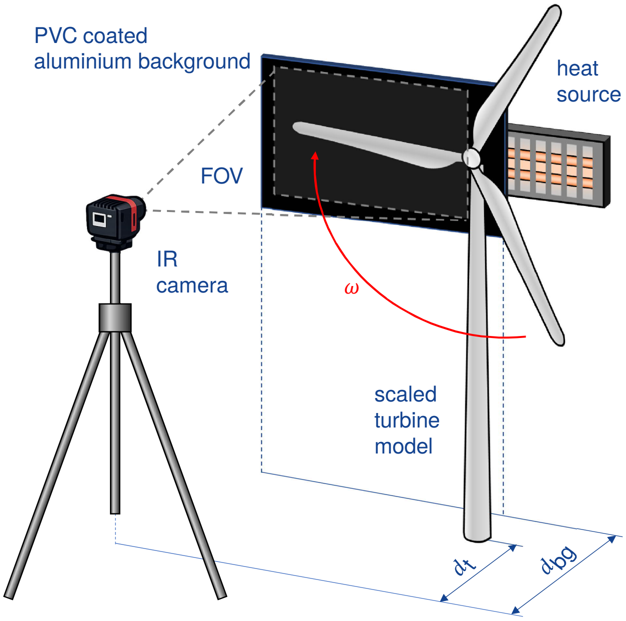

Figure 4. Schematic laboratory setup for the evaluation of motion blur where d_t is the distance between camera and rotor plane, d_bg is the distance between camera and background and ω is the angular velocity of the rotor.

ground is approximately $2\,\mathrm{K}$ to resemble similar contrasts as are observable in laminar–turbulent transitions in the field. Prior to each measurement sequence, thermal equilibrium of the background is verified by monitoring its temporal temperature evolution.

Experimental setup and procedure: Figure 4 shows a schematic of the used laboratory setup. Infrared images are acquired using the camera described in Section 3.1.1. The camera is rigidly mounted on a tripod at a distance d_t of approximately $3.48\,\mathrm{m}$ from the rotor plane, yielding a ground sampling distance of $p_\mathrm{GSD} = 1.17\,\mathrm{mm\,pixel^{-1}}$. By rigid mounting, additional motion or vibration of the camera is excluded, such that relative image motion is solely induced by blade rotation. The distance between camera and background d_bg is $3.84\,\mathrm{m}$. The rotor is driven by an electric motor supplied by a laboratory power supply, allowing adjustment of the rotational speed ω. The applied voltage range lies between $3.5\,\mathrm{V}$ and $14.5\,\mathrm{V}$, corresponding to rotational speeds between approximately $4.3\,\mathrm{min^{-1}}$ and $41.3\,\mathrm{min^{-1}}$. Within individual sequences, rotational-speed fluctuations remain below $2\,\%$ and are assumed to have a negligible influence on the evaluated blur metrics.

Thermograms are recorded for multiple rotational-speed settings and evaluated over nine predefined radial positions to cover a broad range of blade image velocities. For each measurement sequence, thermograms of the entire blade are captured in the camera field of view. The evaluation of the Gaussian error function fit parameter $\hat{w}$ and measurement quantity θ is then performed at each radial position along the blade span.

Data processing and evaluation: In the following, thermograms recorded without rotor motion are referred to as the *static condition*, while thermograms recorded during rotor rotation are referred to as the *dynamic condition*. For each measurement day, a blur-free reference thermogram is acquired once per rotor blade by averaging 100 consecutive frames under static conditions. This reference image provides a high signal-to-noise baseline without motion blur. Thermograms are then recorded during rotation to capture motion-induced image blur. Laboratory data processing follows the general preprocessing and Gaussian error function-based edge-localization framework described in Section 3.1.2. For each blade passage, five frames are acquired in the vicinity of the approximately horizontal blade orientation to obtain comparable edge profiles with minimal out-of-plane motion. Residual vertical offsets between dynamic images and static reference after rotational alignment are minimized using one-dimensional cross-correlation of intensity profiles, ensuring geometric consistency across the evaluated data sets. The used metrics to characterize and quantify the motion-blur effects are explained together with the result descriptions in Sections 4.1 and 4.2, respectively.

3.2.2 Field experiments

Aim of the experiment: The field experiments aim to demonstrate the applicability of UAV-based infrared thermography for flow visualization on an operational wind turbine and to relate the laboratory findings on motion blur to realistic measurement conditions. In contrast to the laboratory experiments, the field measurements are performed under non-repeatable operating conditions and therefore focus on instantaneous transition visualization and qualitative assessment of motion-blur effects rather than on statistical ensemble analysis.

Measurement object: Measurements are performed on a GE 1.5sl wind turbine with a rated power of $1.5\,\mathrm{MW}$, a rotor diameter of $77\,\mathrm{m}$, and a hub height of $68\,\mathrm{m}$. The turbine is operating under normal conditions and aligned into the wind by its yaw control system during the measurement period.

Experimental setup and procedure: Fig. 5 shows the UAV-based measurement system in-flight in front of the investigated turbine. The measurement system is mounted on a hybrid multirotor UAV platform as described in Section 3.1.3. The infrared camera is rigidly mounted on a stabilized gimbal and operated at a frame rate of $25\,\mathrm{Hz}$ with fixed integration time. During the measurements, the UAV is manually positioned at discrete hover locations along the blade span, starting near the hub region and progressing towards the blade tip. At each hover position, the UAV is held approximately stationary while infrared image sequences are recorded over multiple rotor revolutions, corresponding to several blade passages through the camera field of view.

The stand-off distance between the UAV and the rotor blade is estimated from LiDAR data recorded during the flight and evaluated in post-processing. For the measurements reported here, an average camera-to-blade distance of approximately $35\,\mathrm{m}$ is obtained, corresponding to a ground sampling distance of about $11.9\,\mathrm{mm\,pixel^{-1}}$ for the given optical configuration. Rotor speed during the measurements is approximately steady but cannot be actively controlled; it is therefore inferred from the temporal spacing of successive blade passages in the infrared recordings.

Data processing and evaluation: Field data processing follows the general preprocessing and Gaussian error function-based edge-localization framework outlined in Section 3.1.2. In contrast to the laboratory experiments, no static reference image is available under identical conditions, and repeated measurements at exactly the same operating point cannot be obtained. Since the infrared camera does not provide a dedicated hardware trigger input and using a thermal trigger has proven unreliable

Figure 5. UAV in flight during an in-field measurement on an operational wind turbine. The UAV is highlighted by a blue circle and positioned at the pressure side of the rotating rotor, illustrating the measurement geometry and stand-off configuration used during the experiments.

in preliminary tests under airborne conditions, thermograms are recorded in a constant sequence during the flight along the blade positions. As a consequence appropriate images of each hover position are selected manually during post-processing. The thermograms are aligned such that the leading edge is horizontal in the same manner as the images obtained during the laboratory experiments. Evaluation of the transition position and the implications of motion-blur induced deterioration are further detailed in Section 4.3.

4 Results

4.1 Influence of blade image velocity on edge localization

Laboratory experiments are conducted to quantify motion-induced degradation of edge localization under controlled conditions. Thermograms of the complete blade are evaluated at nine radial positions along the span, corresponding to pixel coordinates between $x = 45\,\mathrm{pixel}$ and $x = 441\,\mathrm{pixel}$, which map to physical radii between approximately $150\,\mathrm{mm}$ and $600\,\mathrm{mm}$. Figure 6 compares a motion-free reference thermogram with a frame recorded at a rotor speed of $20\,\mathrm{min}^{-1}$ and indicates the evaluated radial positions with red vertical lines. In the reference image, the blade edges appear sharply defined across the span. In the image from the dynamic condition, the edges become visibly blurred and the blade contour progressively loses definition toward the tip, where the blade image velocity is highest. The detected edges coincide well with the visible blade contour in the static case, but their localization becomes increasingly uncertain under dynamic conditions as motion blur intensifies.

To quantify the blur-induced broadening of the temperature gradients, the width parameter $\hat{w}$ of the Gaussian error function (Eq. 1) is evaluated for both leading edge and trailing edge as a function of blade image velocity v_{img}. Figure 7 (a) shows the mean value of $\hat{w}$ for all evaluated radial positions and operating conditions. Filled markers denote the leading edge, open markers the trailing edge. The error bars represent the standard deviation of the fitted width parameter over the evaluated image sequence. A linear regression is fitted to all data up to a velocity of $v_{\mathrm{img}} = 1000\,\mathrm{pixel\,s}^{-1}$ and shown as a dashed

https://doi.org/10.5194/wes-2026-79
Preprint. Discussion started: 29 May 2026

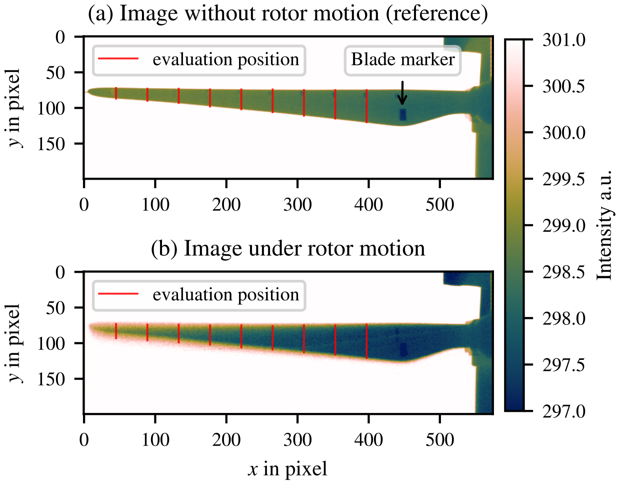

Figure 6. Thermograms of the model rotor blade recorded under static conditions (a) and dynamic conditions at $20\,\mathrm{min}^{-1}$ (b). The images are cropped to a common region of interest, rotated such that the leading edge is horizontal, and the thermogram acquired during rotation is vertically aligned to the motion-free reference. The annotation indicates a blade-identification marker to distinguish individual rotor blades. Radial evaluation positions are indicated by red lines.

line. The linear fit is then extrapolated over the rest of the data points and displayed as a dotted gray line. For both edges, $\hat{w}$ increases approximately linearly with increasing blade image velocity over the entire investigated range, which agrees with the expectation. At $v_{\mathrm{img}} = 1000\,\mathrm{pixel\,s}^{-1}$, the mean edge width reaches approximately $6\,\mathrm{pixel}$, while at $v_{\mathrm{img}} = 2000\,\mathrm{pixel\,s}^{-1}$ it approaches about $12\,\mathrm{pixel}$. The standard deviation of $\hat{w}$ remains comparatively small for blade image velocities below $1000\,\mathrm{pixel\,s}^{-1}$, and the residuals with respect to the linear fit are low. At higher velocities, both the scatter and the deviation from the linear trend increase noticeably.

In order to clarify the reason for the increased uncertainty at large blade image velocities, Fig 8 compares intensity profiles extracted from images taken under static and dynamic conditions at representative blade image velocities. The profiles of the reference image (top) show well-defined constant intensity plateaus and a steep fall and rise at the leading and trailing edge (vertical dotted lines), respectively. The development of the intensity is well-described by the fitted error functions displayed with dashed lines. At a moderate velocity of the rotating blade of $645\,\mathrm{pixel\,s}^{-1}$, as shown in the middle, the Gaussian error function still provides a reasonable approximation of the edge regions. At a higher velocity of $1328\,\mathrm{pixel\,s}^{-1}$ as shown in the bottom, the characteristic profile shape becomes increasingly asymmetric and the chordwise plateau region between leading and trailing edge shrinks substantially. In this regime, the fitted model no longer fully represents the blurred signal, which explains the increased scatter of the width parameter and indicates a limitation of the signal model function under strong motion blur.

(a) Edge width (raw)

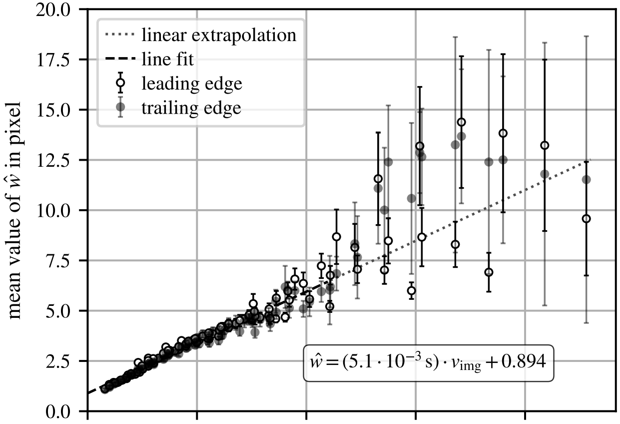

(b) Blade width fluctuation (raw)

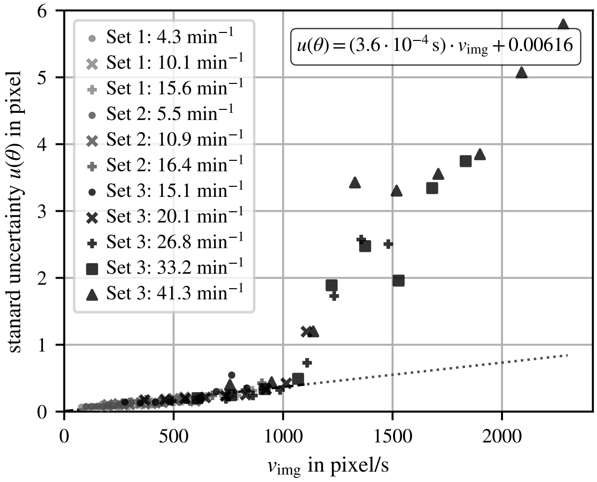

Figure 7. Effect of blade image velocity on the evaluation metrics before deblurring. (a) Mean width parameter $\hat{w}$ of the leading edge (filled symbols) and trailing edge (open symbols) as a function of blade image velocity v_{img}. Error bars indicate the standard deviation. The dashed line shows the linear regression fitted to the data in the low-velocity range, and the dotted line indicates its extrapolation. (b) Estimated standard uncertainty $u(\theta)$ of the transition-location surrogate as a function of blade image velocity v_{img}. For each data point, 100 thermograms are evaluated. Data recorded on three different days are shown in shades of black and gray, while the different rotational speeds evaluated at nine radial positions are distinguished by marker type.

While the broadening of the edge width parameter $\hat{w}$ characterizes the strength of motion blur, the relevant measurand is the transition location θ. Figure 7 (b) shows the standard deviation of the evaluated transition-location surrogate θ as a function of blade image velocity, which is interpreted as an estimate of the standard uncertainty $u(\theta)$. At velocities below $v_{\mathrm{img}} = 1000\,\mathrm{pixel\,s^{-1}}$, the uncertainty increases approximately linearly up to about $0.5\,\mathrm{pixel}$. Beyond this range, the increase continues, but a marked rise in the apparent slope becomes evident, reaching values greater than $5\,\mathrm{pixel}$ for blade image veloci-

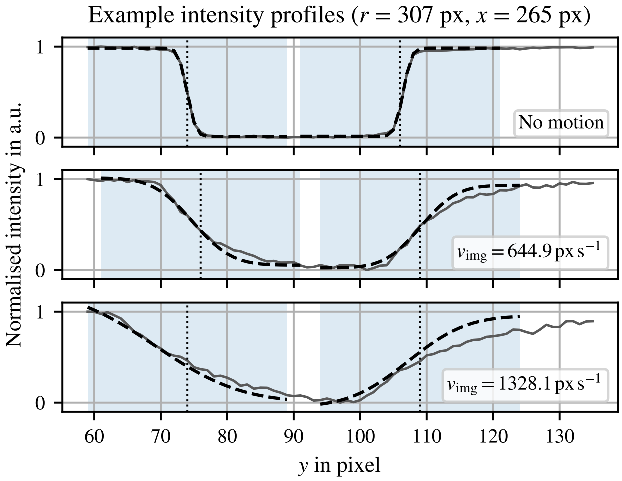

Figure 8. Normalized intensity profiles of the model rotor blade at the radius $r = 307\,\mathrm{pixel}$ for the static condition and rotational speeds $20.1\,\mathrm{min}^{-1}$ and $41.3\,\mathrm{min}^{-1}$, resulting in blade image velocities of $645\,\mathrm{pixel\,s^{-1}}$ and $1328\,\mathrm{pixel\,s^{-1}}$, respectively. Solid gray lines show row-wise intensity data averaged over five pixels. Dashed lines show the Gaussian error function fits of the leading and trailing blade edges evaluated over the y-coordinates highlighted with light blue background. The calculated edge positions are depicted with vertical dotted lines.

ties above $2000\,\mathrm{pixel\,s^{-1}}$. This behaviour is consistent with the profile deformation discussed above and indicates a progressive loss of localization robustness with increasing motion blur. Because both leading and trailing edges in the laboratory data exhibit comparable thermal contrast, the determined uncertainty $u(\theta)$ due to motion blur serves as a conservative estimation when transferred to field conditions, where the leading edge is typically more sharply defined than the laminar–turbulent transition. However, the laboratory results demonstrate that motion blur alone can impose a substantial limitation on transition localization under realistic operating conditions.

4.2 Image deblurring and mitigation strategies

In order to minimize transition localization uncertainty due to motion blur, image deblurring can be applied prior to the edge-detection procedure. In the present study, deblurring is performed using deconvolution methods following the approach proposed by Oswald-Tranta et al. (2010). In this method, the motion blur caused by the finite temporal response of the microbolometer detector is represented by a point-spread function (PSF) derived from the detector's exponential response. The thermograms are restored by Wiener deconvolution of the raw thermograms, i.e. before the geometric preprocessing and edge evaluation steps are applied.

To estimate the image motion required for the PSF model, the rotational motion of the blade is isolated in the image plane. The center of rotation is manually selected once per measurement run and defined by the pixel coordinates of the hub in the thermograms. Since neither the camera nor the turbine position changes during a measurement sequence, this center remains constant for all frames of a given run. The angular velocity ω is estimated from the time intervals between consecutive blade passages detected in the infrared image sequence. For each operating condition, the mean value obtained from all recorded rotations is used for the subsequent evaluation.

Under the assumption that the dominant motion occurs tangentially in the image plane, the thermograms are transformed into polar coordinates using the polar remapping functionality provided by OpenCV (`warpPolar`; Bradski, 2000). In this representation, the rotational blade motion is mapped onto a one-dimensional displacement along the angular coordinate, which allows the motion blur to be approximated by a one-dimensional PSF. A related motion-flow-based deblurring approach for infrared thermograms of rotating wind turbine blades was recently proposed by Liu et al. (2025), using segmented blade regions to account for spatially varying motion.

Following Oswald-Tranta et al. (2010), the PSF is modeled as an exponential decay corresponding to the first-order temporal response of the microbolometer detector,

$$h(m) = \frac{1}{s_{\mathrm{pixel}}} \exp\left(-\frac{m}{s_{\mathrm{pixel}}}\right), \tag{5}$$

where m denotes the discrete pixel lag along the direction of motion and s_{pixel} is the characteristic blur length in pixels. The latter is obtained from the image-plane velocity and the detector time constant, $s_{\mathrm{pixel}} = v_{\mathrm{pixel}}\,\tau$, with $v_{\mathrm{pixel}} = \omega \frac{N_\theta}{2\pi}$, where N_θ denotes the number of angular pixels in the polar representation and τ is the detector time constant. The detector time constant is taken as $\tau = 11\,\mathrm{ms}$ according to the manufacturer specification of the infrared camera. The blur in the thermograms is then compensated using Wiener deconvolution,

$$\hat{F} = F^{-1}\left(\frac{|H|^2}{|H|^2 + k}\left(F + \frac{N}{H}\right)\right), \tag{6}$$

where H denotes the Fourier transform of the PSF, N represents the Fourier transform of the noise influence and k is a regularization parameter controlling the influence of noise amplification. The parameter k is treated as a constant value in the present implementation and set to $k = 0.005$.

Figure 9 presents the results obtained after applying Wiener deconvolution prior to edge detection. Subplot (a) shows the fitted edge-width parameter as a function of blade image velocity, while subplot (b) shows the resulting standard uncertainty of the transition-location metric θ. The evaluation procedure follows the same methodology as described in Section 4.1, and the axis limits are kept identical to those used previously in order to allow direct comparison with the undeconvolved results in Fig. 7.

The edge-width results in Fig. 9 (a) still exhibit an approximately linear increase with blade image velocity. Compared with the raw thermograms, however, the slope of this increase is significantly reduced, the edge widths at high blade image velocities are reduced by one order of magnitude and the variability of the fitted parameter is smaller. In particular, the fitted edge widths remain below approximately $2.5\,\mathrm{pixel}$ over most of the velocity range up to blade image velocities of about $2300\,\mathrm{pixel\,s^{-1}}$. The standard deviations represented by the error bars also remain small throughout most of the investigated range. This reduction in variability indicates that the Gaussian error-function model can represent the restored edge profiles more consistently after deblurring.

(a) Edge width (deblurred)

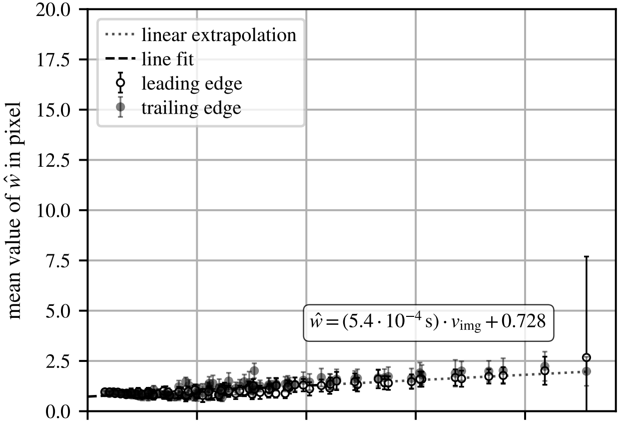

(b) Blade width fluctuation (deblurred)

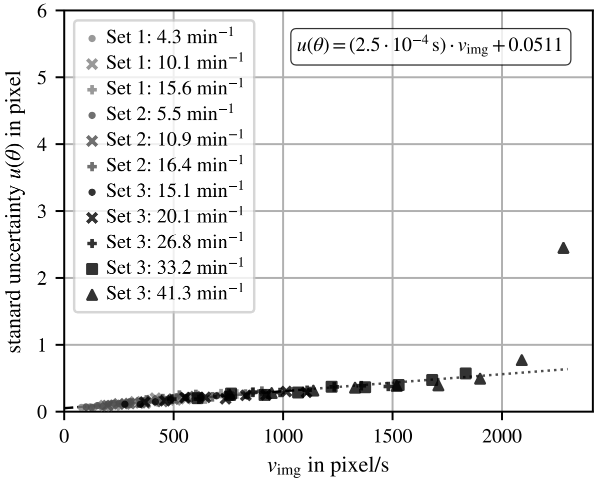

Figure 9. Effect of Wiener deconvolution on the evaluation metrics as a function of blade image velocity. (a) Mean edge-width parameter $\hat{w}$ for the leading edge (filled symbols) and trailing edge (open symbols). Error bars indicate the standard deviations and the dashed line shows a linear regression fitted to all data. (b) Standard uncertainty of the transition-location metric θ. The evaluation is performed using the same methodology as in Section 4.1, and the axis limits are kept identical to those of Fig. 7 to allow direct comparison with the undeconvolved results.

The leading and trailing edges follow similar overall trends, although the trailing-edge widths appear consistently slightly larger than those of the leading edge. The final data points at the highest velocities still follow the general linear trend but show increased scatter. This increase in variability is attributed to artifacts introduced by the deconvolution process near the blade tips, where parts of the background can be mapped onto the blade region during deblurring (see Fig. 10). Such distortions affect the edge-detection procedure and lead to larger fluctuations of the fitted parameters.

The effect of deblurring on the transition-location uncertainty is shown in Fig. 9 (b). In analogy to Section 4.1, the standard deviation of the evaluated transition-location surrogate θ is interpreted as an estimate of the standard uncertainty $u(\theta)$. The uncertainty $u(\theta)$ follows an approximately linear trend over the full investigated velocity range, but with a clearly reduced slope compared with the undeconvolved data in Fig. 7. The sudden increase in slope observed in the undeconvolved data is no longer present. In particular, the standard deviation of θ remains below approximately $1\,\mathrm{pixel}$ over the entire range of blade image velocities. At $v_{\mathrm{img}} \approx 2000\,\mathrm{pixel\,s^{-1}}$, this corresponds to an improvement by roughly a factor of five compared with the original evaluation, where the uncertainty exceeded $5\,\mathrm{pixel}$. Only the final data point at the highest velocity shows a noticeable deviation from the trend, which is consistent with the artifact-related fluctuations already observed in the edge-width evaluation.

To illustrate the origin of the remaining deviations, Fig. 10 compares representative thermograms before and after deblurring. The upper image shows a representative frame from the measurement run at $41.3\,\mathrm{min^{-1}}$, which corresponds to the highest investigated blade image velocities. The blade contour appears strongly blurred and the outline of the blade tip becomes difficult to distinguish. The lower image shows the corresponding thermogram after Wiener deconvolution. While the restored image exhibits increased noise compared with the original frame, the blade edges appear sharper and the contrast between blade and background is largely recovered. A slight reduction in the overall intensity level can also be observed in the restored image. An artifact of the deconvolution process is visible in the upper-left region of the restored image, where a boundary of the background is mapped across the blade tip. Such artifacts originate from the deconvolution and polar remapping steps and can affect the edge-detection procedure when they intersect the blade region. However, for images in which the blade is captured close to the intended horizontal orientation, these artifacts typically remain outside the region of interest used for the evaluation. Only frames with a larger angular offset exhibit this behavior, which explains the increased variability observed for the highest blade image velocities in Fig. 9.

4.3 Field measurements and operational implications

Qualitative field evaluation. The laboratory investigations presented in Sections 4.1 and 4.2 showed that motion blur is a dominant factor limiting the localization of transition-like features in thermographic images and that its effect can be reduced by image deblurring. Field measurements on an operating wind turbine involve additional complexities, including varying viewing geometry, changing environmental conditions, and the absence of repeatable operating states. This section therefore examines how the motion-blur-related limitations identified in the laboratory appear under field conditions and how deblurring affects the visibility and evaluability of transition signatures in the field data.

Representative thermograms from individual hover positions are stitched into a combined view of the blade, which serves as a positional reference for the subsequent evaluation. Because distinct surface features are largely absent, an area-based image alignment method based on the enhanced correlation coefficient is used (Evangelidis and Psarakis, 2008), employing the corresponding implementation in OpenCV (Bradski, 2000). The stitched image is used to identify the center of rotation at the hub and to infer the spanwise radial position of the evaluated profiles. Rotor speed is estimated from the time interval between successive blade passages, which, together with the radial position, yields the blade image velocity. Based on the

https://doi.org/10.5194/wes-2026-79
Preprint. Discussion started: 29 May 2026

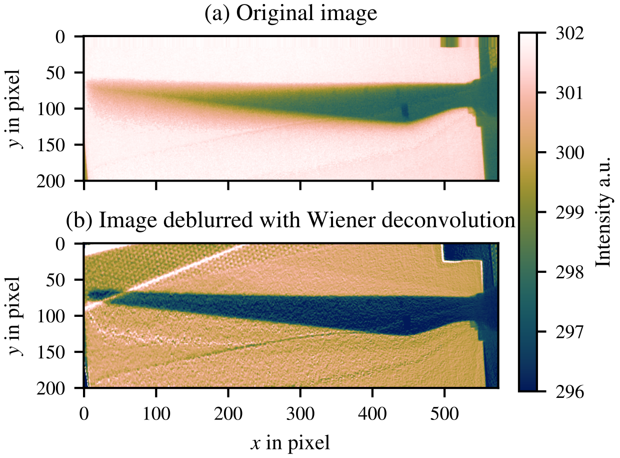

Figure 10. Example thermograms of the model rotor blade before and after deblurring by Wiener deconvolution. The image in (a) shows a preprocessed and cropped frame recorded at a rotational speed of $41.3\,\mathrm{min}^{-1}$, exhibiting strong motion blur and a barely distinguishable blade tip. The image in (b) shows the corresponding restored frame after deconvolution. The blade edges appear substantially sharpened and the contrast between blade and background is increased, while the restored image also exhibits elevated noise and an artifact in which the background is mapped across the blade tip.

estimated center of rotation, Wiener deconvolution is applied to the individual thermograms, and the deblurred images are stitched again using the same procedure.

A representative result is shown in Fig. 11, which presents stitched thermograms of the blade before and after deblurring. The measurements were acquired under mostly clear-sky conditions, but wind speeds were low and variable, and the turbine repeatedly entered and left operation. A fully developed and stationary boundary-layer state therefore cannot be assumed over the entire blade. In addition, the blades contain tripping elements, which may affect both the flow state and the thermal signature.

Before deblurring, a transition-related thermal signature with turbulent wedges is visible mainly over the inner part of the blade, whereas motion blur increasingly reduces edge sharpness towards the tip. Fine structures remain visible near the hub, indicating that the loss of sharpness at larger radial positions is primarily caused by image motion rather than defocus. After Wiener deconvolution, the blade edges appear sharper over a much larger spanwise range, and faint wedge-like structures become visible further outboard. At the same time, the restored thermograms exhibit increased noise and isolated artifacts, including a lower-temperature stripe of unresolved origin. Overall, the field images indicate that motion blur is the main factor limiting transition detectability at larger radial positions and that deblurring can recover transition-related structures that are otherwise obscured.

Image-based uncertainty estimate. Beyond this qualitative improvement in transition visibility, the field data also permit an image-based estimate of the uncertainty of the inferred transition position θ/c defined in Eq. (4). In principle, the uncertainty

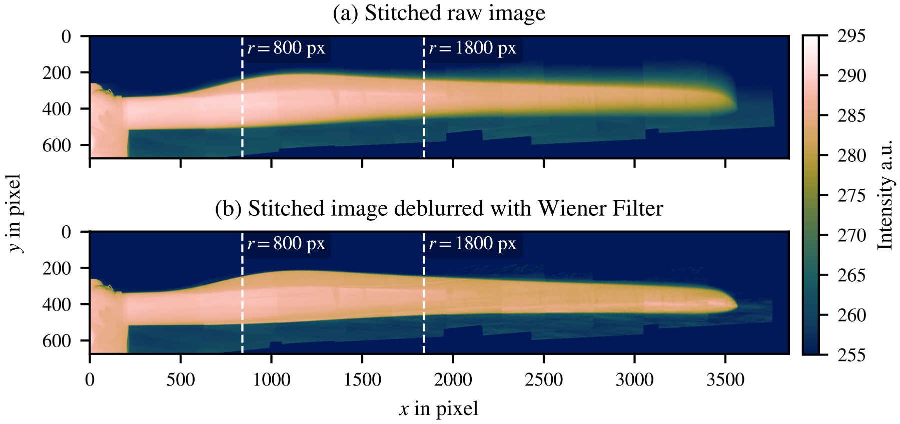

Figure 11. Stitched thermograms of the rotor blade recorded under field conditions. Radial positions for the evaluation of the positional uncertainty are shown with white dashed lines. (a) Raw thermograms prior to deblurring. A characteristic transition signature with turbulent wedges is visible over approximately the inner half of the blade, while motion blur increasingly obscures the blade edges towards the tip. (b) Thermograms after Wiener deconvolution. The blade edges appear sharper and with higher contrast along the full span, and faint turbulent wedge structures become visible in the tip region. The restored image exhibits increased noise.

of this quantity depends on the position uncertainty of the leading edge, trailing edge, and laminar–turbulent transition. In the present case, however, the dominant uncertainty contribution is assumed to arise from the transition position, because the blade edges exhibit much higher contrast and sharper gradients than the transition signature. By neglecting $u(\hat{b}_{\mathrm{LE}})$ and $u(\hat{b}_{\mathrm{TE}})$, the uncertainty propagation calculation for Eq. (4) results in $u(\theta/c) \approx u(\hat{b}_{\mathrm{LTT}})/c$.

To obtain $u(\hat{b}_{\mathrm{LTT}})$, the analytical expression derived by Fischer (2026) for transition profiles described by a Gaussian error function is used. Adapting Eq. (9) of Fischer (2026) to the present notation, it is

$$u(\hat{b}_{\mathrm{LTT}}) \geq \sqrt{2\sqrt{\pi}}\,\frac{\sqrt{\hat{w}_{\mathrm{LTT}}\,\Delta y}}{\eta_{\mathrm{LTT}}}. \tag{7}$$

Here, $\hat{w}_{\mathrm{LTT}}$ denotes the fitted width of the transition profile, Δy is the sampling interval along the evaluated profile, and η_{LTT} is the local contrast-to-noise ratio of the transition signature. In the present evaluation, $\Delta y = 1\,\mathrm{pixel}$ and $\eta_{\mathrm{LTT}} = 2\,|\hat{a}_{\mathrm{LTT}}|/\sigma_I$, where $\hat{a}_{\mathrm{LTT}}$ is the fitted amplitude in Eq. (1). The noise level σ_I is estimated from the two-dimensional normalized stripe data by broadcasting the fitted one-dimensional error-function profile over the stripe width and evaluating the standard deviation of the residuals in the sideband region

$$\hat{w}_{\mathrm{LTT}} \leq |y - \hat{b}_{\mathrm{LTT}}| \leq \hat{w}_{\mathrm{LTT}} + 20\,\mathrm{pixel}.$$

This excludes the transition core while remaining close to the transition. For strongly blurred profiles, the residuals may include model mismatch in addition to image noise. Consequently, σ_I is interpreted as an effective residual level, and the resulting uncertainty estimate is considered most meaningful for deblurred profiles, where the fitted model represents the measured transition shape more consistently.

Table 1. Estimated quantities used for the uncertainty evaluation at two representative radial positions in the field data before and after Wiener deconvolution.

		$r = 800$ pixel		$r = 1800$ pixel	
Quantity	unit	raw	deblurred	raw	deblurred
v_{img}	pixel s^{-1}	930	930	2092	2092
$\hat{w}_{\mathrm{LTT}}$	pixel	9.3	5.5	16.3	4.0
η_{LTT}	–	18.7	8.8	7.1	6.5
σ_I	–	0.052	0.096	0.166[1]	0.097
$\hat{a}_{\mathrm{LTT}}$	–	0.487	0.422	0.590[1]	0.313
c	pixel	258	261	204	212
θ	pixel	70.0	74.1	71.3	70.4
$u(\hat{b}_{\mathrm{LTT}})$	pixel	0.31	0.50	1.07	0.58
$u(\theta/c)$	%	0.12	0.19	0.53	0.27

1: Elevated values of σ_I and $\hat{a}_{\mathrm{LTT}}$ indicate model mismatch between the fitted error function and the deformed transition profile.

In order to estimate the transition position uncertainty, two representative transition profiles are evaluated at the radial positions marked in Fig. 11, namely $r = 800\,\mathrm{pixel}$ and $r = 1800\,\mathrm{pixel}$, for a rotor speed of $11\,\mathrm{min}^{-1}$, see Table 1. At the inner radial position ($r = 800\,\mathrm{pixel}$), the raw profile exhibits a moderate blade image velocity of $930\,\mathrm{pixel\,s}^{-1}$, with a fitted transition width of $9.3\,\mathrm{pixel}$ and a comparatively high contrast-to-noise ratio of 18.7. This results in a low estimated uncertainty of $u(\theta/c) = 0.12\,\%$. After deblurring, the transition width is reduced to $5.5\,\mathrm{pixel}$, indicating a clear sharpening of the transition signature. However, the noise level increases, leading to a reduction in contrast-to-noise ratio to 8.8 and a slight increase in uncertainty to $0.19\,\%$. This behavior suggests that, at moderate blade image velocities, the Gaussian error-function model already provides a robust representation of the measured profiles, and the noise amplification introduced by the deconvolution outweighs the benefit of reduced gradient width. A small shift in the estimated transition position θ is also observed, indicating that deblurring may influence not only the gradient sharpness but also the fitted position.

At the outer radial position ($r = 1800\,\mathrm{pixel}$), corresponding to a higher blade image velocity of $2092\,\mathrm{pixel\,s}^{-1}$, the raw profile is strongly affected by motion blur. This is reflected in the large fitted transition width of $16.3\,\mathrm{pixel}$ and the comparatively low contrast-to-noise ratio of 7.1, resulting in a substantially increased uncertainty of $u(\theta/c) = 0.53\,\%$. The elevated noise level ($\sigma_I = 0.166$) indicates that the fitted model does not adequately represent the distorted profile shape and should therefore be interpreted as a manifestation of model mismatch rather than purely increased image noise. This interpretation is consistent with the comparatively large fitted amplitude $\hat{a}_{\mathrm{LTT}}$, which suggests an overestimation of the transition step height under strong blur conditions. After deblurring, the transition width is reduced to $4.0\,\mathrm{pixel}$, while the contrast-to-noise ratio decreases only slightly to 6.5. In contrast to the inner position, the dominant effect of deblurring at high blade image velocities is therefore the restoration of a physically meaningful profile shape. This leads to a more consistent representation by the Gaussian error-function model and, consequently, to a more robust estimation of the transition location, despite moderate noise amplification. These observations are in line with the laboratory results presented in Section 4.1, where increasing blade image velocity led to a progressive deviation of the measured profiles from the assumed model shape. The field data confirm that this model mismatch becomes the dominant source of uncertainty at high v_{img}, and that deblurring primarily improves the applicability of the signal model rather than simply reducing gradient width. The use of blade image velocity as a governing parameter thus provides a consistent framework for interpreting motion-blur effects across laboratory and field conditions. The obtained uncertainty levels are within the same order of magnitude as those reported for ground-based infrared thermography under controlled conditions, where Dollinger et al. (2018) achieved uncertainties of approximately $0.17\,\%$ of the chord length. This comparison indicates that, despite the additional challenges associated with UAV-based measurements, comparable levels of accuracy can be approached when motion-blur effects are properly accounted for.

5 Conclusions

The present study investigated the applicability of UAV-based infrared thermography for aerodynamic flow visualization on operational wind turbines, with particular focus on the localization of the laminar–turbulent transition. The results showed that the thermal transition signature can be captured with a lightweight microbolometer camera under field conditions on a megawatt-scale wind turbine, but that the quantitative localization capability is strongly constrained by motion blur induced by high blade image velocity.

Laboratory experiments isolated this effect and confirmed that increasing blade image velocity progressively broadens the apparent edge gradients and increases the uncertainty of the transition-location surrogate θ. The Gaussian error-function model used for both edge and transition localization remained applicable at moderate image velocities, but its robustness deteriorated strongly once the blurred profiles no longer resembled the underlying edge shape. In this regime, motion blur alone imposed a substantial limitation on the localization uncertainty $u(\theta)$.

Applying Wiener deconvolution following Oswald-Tranta et al. (2010) to compensate motion blur effects substantially improved the evaluation. In the laboratory data, the deblurred thermograms show markedly reduced edge broadening and a strong reduction in transition-location uncertainty, with an improvement by approximately a factor of five at high blade image velocities. The field measurements confirmed this improvement qualitatively: after deblurring, blade edges remain visible across a much larger portion of the span and faint transition-related structures become discernible even in regions where they were obscured in the original thermograms. Field data further indicate that this improvement is primarily associated with restoring the validity of the signal model under strong motion blur, while at moderate blade image velocities the benefit may be partly offset by increased noise levels.

The field investigation also highlighted that motion blur is not the only relevant limitation under operational conditions. Variable turbine operation and incomplete knowledge of blade geometry restrict the interpretation of the thermograms and the direct assessment of uncertainty. Nevertheless, the laboratory-derived relationship between blade image velocity and localization uncertainty provides a physically motivated and conservative estimate of the motion-blur-induced uncertainty contribution in the field.

Overall, the study demonstrated that UAV-based IRT is a viable approach for transition visualization on operational wind turbines and can reach uncertainty values comparable with ground based setups, provided that motion-blur effects are explicitly considered and mitigated. Future work should focus on improved geometric referencing, inclusion of camera motion in the uncertainty evaluation, and parallel reference measurements with motion-blur-free ground-based systems to further strengthen the quantitative interpretation of airborne thermographic flow measurements.

Code and data availability. The raw data as well as the evaluation algorithms supporting the conclusion of this article will be made available by the authors upon reasonable request, without undue reservation.

Author contributions. LR: Conceptualization, Methodology, Investigation (laboratory and field experiments), Data curation, Software, Validation, Formal analysis, Writing – original draft, Project administration. NP: Investigation (field experiments), Data curation, Software, Validation. NB: Conceptualization, Writing – review & editing. AvF: Methodology, Formal analysis, Writing – review & editing, Supervision. AF: Conceptualization, Methodology, Formal analysis, Writing – review & editing, Supervision.

Competing interests. The authors declare that they have no conflict of interest.

Disclaimer. The views expressed in this article are those of the authors and do not necessarily reflect the views of Deutsche WindGuard Engineering GmbH or other affiliated institutions.

Acknowledgements. This research is financed by the Federal Ministry for Economic Affairs and Energy (BMWE) grant number 03EE3064A.

During the preparation of this work, the author used ChatGPT5 to draft parts of the text and to improve the code used for data evaluation. After using this tool/service, the author reviewed and edited the content as needed and takes full responsibility for the content of the publication.

References

Bradski, G.: The OpenCV Library, Dr. Dobb's Journal of Software Tools, 2000.

Burgmann, S., Brücker, C., and Schröder, W.: Scanning PIV measurements of a laminar separation bubble, Experiments in Fluids, 41, 319–326, https://doi.org/10.1007/s00348-006-0153-6, 2006.

Chaudhuri, S., Stamm, M., Lapšanská, I., Lançon, T., Osterbrink, L., Driebe, T., Hein, D., and Harendt, R.: Infrared Thermography of Turbulence Patterns of Operational Wind Turbine Rotor Blades Supported With High–Resolution Photography: KI–VISIR Dataset, Wind Energy, 28, https://doi.org/10.1002/we.2958, 2024.

Chen, Q., Yang, R., Liu, X., Deng, B., Wang, H., and He, Y.: A review on flow visualisation of wind turbine blades in operation, Nondestructive Testing and Evaluation, pp. 1–22, https://doi.org/10.1080/10589759.2025.2466813, 2025.

Costantini, M., Henne, U., Risius, S., and Klein, C.: A robust method for reliable transition detection in temperature-sensitive paint data, Aerospace Science and Technology, 113, 106 702, https://doi.org/10.1016/j.ast.2021.106702, 2021.

Crameri, F.: Scientific colour maps, https://doi.org/10.5281/zenodo.1243862, 2018.

Dollinger, C., Sorg, M., Balaresque, N., and Fischer, A.: Measurement uncertainty of IR thermographic flow visualization measurements for transition detection on wind turbines in operation, Experimental Thermal and Fluid Science, 97, 279–289, https://doi.org/10.1016/j.expthermflusci.2018.04.025, 2018.

Dorszewski, C., Dieckmann, J., Balaresque, N., von Freyberg, A., and Fischer, A.: Weather-dependency of the thermographic flow visualization of the laminar-turbulent transition on wind turbines, Measurement Science and Technology, 35, 095 301, https://doi.org/10.1088/1361-6501/ad4d11, 2024.

Evangelidis, G. D. and Psarakis, E. Z.: Parametric image alignment using enhanced correlation coefficient maximization, IEEE transactions on pattern analysis and machine intelligence, 30, 1858–1865, https://doi.org/10.1109/TPAMI.2008.113, 2008.

Fischer, A.: Thermography-based localisation of laminar-turbulent transition on airfoils: a fundamental limit of measurability, Quantitative InfraRed Thermography Journal, pp. 1–16, https://doi.org/10.1080/17686733.2026.2616874, 2026.

Fischer, A., Parrey, A.-M., Balaresque, N., and von Freyberg, A.: Flow visualization by means of 3D thermography on yawing wind turbines, Frontiers in Energy Research, 11, https://doi.org/10.3389/fenrg.2023.1240183, 2023.

Galleguillos, C., Zorrilla, A., Jimenez, A., Diaz, L., Montiano, Á. L., Barroso, M., Viguria, A., and Lasagni, F.: Thermographic non-destructive inspection of wind turbine blades using unmanned aerial systems, Plastics, Rubber and Composites, 44, 98–103, https://doi.org/10.1179/1743289815Y.0000000003, 2015.

Gartenberg, E., Johnson, W. G., Wright, R. E., Carraway, D. L., and Johnson, C. B.: Boundary-layer transition-detection in a cryogenic wind tunnel usinginfrared imaging, AIAA Journal, 30, 444–446, https://doi.org/10.2514/3.10936, 1992.

Gleichauf, D., Dollinger, C., Balaresque, N., Gardner, A. D., Sorg, M., and Fischer, A.: Thermographic flow visualization by means of non-negative matrix factorization, International Journal of Heat and Fluid Flow, 82, 108 528, https://doi.org/10.1016/j.ijheatfluidflow.2019.108528, 2020.

Gleichauf, D., Oehme, F., Sorg, M., and Fischer, A.: Laminar-Turbulent Transition Localization in Thermographic Flow Visualization by Means of Principal Component Analysis, Applied Sciences, 11, 5471, https://doi.org/10.3390/app11125471, 2021.

Gleichauf, D., Oehme, F., Parrey, A.-M., Sorg, M., Balaresque, N., and Fischer, A.: On-site contactless visualization of the laminar-turbulent flow transition dynamics on wind turbines, tm - Technisches Messen, 90, 613–623, https://doi.org/10.1515/teme-2022-0120, 2023.

Herráez, I., Daniele, E., and Schepers, J. G.: Extraction of the wake induction and angle of attack on rotating wind turbine blades from PIV and CFD results, Wind Energy Science, 3, 1–9, https://doi.org/10.5194/wes-3-1-2018, 2018.

Joseph, L. A., Borgoltz, A., and Devenport, W.: Infrared thermography for detection of laminar–turbulent transition in low-speed wind tunnel testing, Experiments in Fluids, 57, https://doi.org/10.1007/s00348-016-2162-4, 2016.

Jung, C., Sander, L., and Schindler, D.: Future global offshore wind energy under climate change and advanced wind turbine technology, Energy Conversion and Management, 321, 119 075, https://doi.org/10.1016/j.enconman.2024.119075, 2024.

Li, Q., Kamada, Y., Maeda, T., Murata, J., and Nishida, Y.: Visualization of the flow field and aerodynamic force on a Horizontal Axis Wind Turbine in turbulent inflows, Energy, 111, 57–67, https://doi.org/10.1016/j.energy.2016.05.098, 2016.

Liu, T., Sullivan, J. P., Asai, K., Klein, C., and Egami, Y.: Pressure and Temperature Sensitive Paints, Springer International Publishing, Cham, https://doi.org/10.1007/978-3-030-68056-5, 2021.

Liu, X., Yang, R., Chen, Q., Deng, B., Jin, M., Wang, F., and He, Y.: Deblur of Infrared Thermal Images of In-Service Wind Turbine Blade Based on Rotational Motion Flow, SSRN [preprint], https://doi.org/10.2139/ssrn.5899715, 2025.

Medina, P., Schreck, S., Johansen, J., and Fingersh, L.: Oil-flow visualization on a SWT-2.3-101 wind turbine, in: 29th AIAA Applied Aerodynamics Conference, American Institute of Aeronautics and Astronautics, Reston, Virigina, ISBN 978-1-62410-145-8, https://doi.org/10.2514/6.2011-3818, 2011a.

Medina, P., Singh, M., Johansen, J., Rivera Jove, A., Machefaux, E., Fingersh, L., Shreck, S., and (None): Aerodynamic and Performance Measurements on a SWT-2.3-101 Wind Turbine, in: Proceedings of WINDPOWER 2011 Conference & Exhibition, vol. NREL/CP-5000-51649, NREL National Renewable Energy Laboratory, https://docs.nrel.gov/docs/fy12osti/51649.pdf, 2011b.

Montelpare, S. and Ricci, R.: A thermographic method to evaluate the local boundary layer separation phenomena on aerodynamic bodies operating at low Reynolds number, International Journal of Thermal Sciences, 43, 315–329, https://doi.org/10.1016/j.ijthermalsci.2003.07.006, 2004.

Oehme, F., Gleichauf, D., Balaresque, N., Sorg, M., and Fischer, A.: Thermographic detection and localisation of unsteady flow separation on rotor blades of wind turbines, Frontiers in Energy Research, 10, https://doi.org/10.3389/fenrg.2022.1043065, 2022a.

Oehme, F., Gleichauf, D., Suhr, J., Balaresque, N., Sorg, M., and Fischer, A.: Thermographic detection of turbulent flow separation on rotor blades of wind turbines in operation, Journal of Wind Engineering and Industrial Aerodynamics, 226, 105 025, https://doi.org/10.1016/j.jweia.2022.105025, 2022b.

Oswald-Tranta, B., Sorger, M., and O'Leary, P.: Motion deblurring of infrared images from a microbolometer camera, Infrared Physics & Technology, 53, 274–279, https://doi.org/10.1016/j.infrared.2010.04.003, 2010.

Reichstein, T., Schaffarczyk, A. P., Dollinger, C., Balaresque, N., Schülein, E., Jauch, C., and Fischer, A.: Investigation of Laminar–Turbulent Transition on a Rotating Wind-Turbine Blade of Multimegawatt Class with Thermography and Microphone Array, Energies, 12, 2102, https://doi.org/10.3390/en12112102, 2019.

Reyer, M., Rudolph, I., and Nitsche, W.: Investigations into the Visualization and Quantification of Wall Shear Stress Distributions Using Infrared Thermography, in: 25th AIAA Aerodynamic Measurement Technology and Ground Testing Conference, American Institute of Aeronautics and Astronautics, Reston, Virigina, ISBN 978-1-62410-029-1, https://doi.org/10.2514/6.2006-3840, 2006.

Schaffarczyk, A. P., Schwab, D., and Breuer, M.: Experimental detection of laminar–turbulent transition on a rotating wind turbine blade in the free atmosphere, Wind Energy, 20, 211–220, https://doi.org/10.1002/we.2001, 2017.

Schlichting, H. and Gersten, K.: Boundary-Layer Theory, Springer Berlin Heidelberg, Berlin, Heidelberg, https://doi.org/10.1007/978-3-662-52919-5, 2017.

Traphan, D., Herráez, I., Meinlschmidt, P., Schlüter, F., Peinke, J., and Gülker, G.: Remote surface damage detection on rotor blades of operating wind turbines by means of infrared thermography, Wind Energy Science, 3, 639–650, https://doi.org/10.5194/wes-3-639-2018, 2018.

Vey, S., Lang, H. M., Nayeri, C. N., Paschereit, C. O., and Pechlivanoglou, G., eds.: Extracting quantitative data from tuft flow visualizations on utility scale wind turbines, vol. 524, https://doi.org/10.1088/1742-6596/524/1/012011, 2014.